10.7 A 0.3ppm Dual-Resonance Transformer-Based Drift-Cancelling Reference-Free Magnetic Sensor for Biosensing Applications

Constantine Sideris, Parham Porsandeh Khial, Bill Ling, Ali Hajimiri

California Institute of Technology, Pasadena, CA

Cost-efficient, point-of-use diagnostics are critical for early disease detection. Traditionally, the majority of lab-based analysis equipment utilizes fluorescent markers for biodetection assays. However, magnetic-based labels have recently been shown to be promising alternatives to fluorescent tags for DNA, protein, and cell assays. Magnetic assays offer several key advantages over their fluorescent counterparts, namely that magnetic beads do not suffer from signal decay due to bleaching and that they can be detected with cheap CMOS-based sensors, eliminating the need for expensive lasers, photo-diodes, filters, and complicated post-processing steps. Significant progress has recently been made in the design of magnetic imager ICs, such as [1] which utilizes a GMR approach for detection and [2-4] which measure the resonance shift in an LC tank.

While LC-based approaches arguably offer the simplest and cheapest approach for detecting magnetic labels, they suffer major drift issues due to the fact that the resonance shift in the LC tank is typically sensed by measuring the frequency-shift of an on-chip, free-running oscillator. Utilizing a replica reference can compensate a few sources of drift; however, this consumes twice the amount of power and chip area. Further, thermal gradients on the chip and noise sources of the active devices lead to major degradation in SNR for long-term measurements and cannot be adequately cancelled with a replica reference. In-vitro experiments must often be carried out over multiple hour-long timescales, making the original LC detection approach impractical for realistic assays. Other approaches for compensating drift in LC-based sensors require external permanent magnets and moving parts and may still require replica reference sensors.

The work in [4] achieves magnetic multiplexing by taking advantage of the rich frequency dependence of the magnetic susceptibility of magnetic nanoparticles. Notably, the nanoparticles contribute negatively beyond a certain excitation frequency and decrease the total sensor inductance. At high enough frequencies, the particles become transparent to the polarizing field and do not affect the effective sensing inductance. Therefore, designing a dual-frequency oscillator enables measurement of the contribution of the beads at the lower frequency and tracking of the sensor drift at the higher frequency, where the beads are transparent and do not affect the oscillation frequency. A switched-capacitor-based topology, as in [4], is one potential approach for achieving two oscillation frequencies with the same sensing inductor cell. Unfortunately, the higher frequency of oscillation would not utilize the majority of the tank capacitance used by the lower frequency making it a poor approach for accurately tracking the drift of the lower frequency. Moreover, the switches required to switch the extra tank capacitors would have to be very large to achieve sufficiently low on-resistance, adding a significant amount of extra parasitic capacitance and contributing more noise to the system.

Instead, we consider the 4th-order transformer-based system shown in Fig. 10.7.1. This 4th-order tank has two resonance frequencies, whose ratios can be shown to depend as: $f_1 / f_2 = \sqrt{(1 - k) / (1 + k)}$ when $L_1C_1=L_2C_2$, where k is the transformer coupling factor. In this work, we exploit the dependence of this ratio only on k, which desensitizes the system to variations in other component values (e.g., tank capacitance and device parasitics). The low and high resonances of the tank represent symmetric and anti-symmetric modes of the transformer and result in the primary and secondary oscillation voltages being in phase and 180° out of phase respectively. In order for the system to oscillate at the desired frequency, switches can be used as shown in Fig. 10.7.1 to enforce the required boundary conditions. Unlike the switches required for switched-capacitor-based topologies, the node voltages on both sides of these switches are always identical, indicating that they do not pass any current and thus do not contribute to the overall system noise or tank capacitance.

The transformer-based system can thus oscillate at both the low and high frequencies depending on switch setting, and in the absence of magnetic particles over the transformer surface, the two frequencies will track each other with a ratio depending only on the transformer k, as noted earlier. The presence of magnetic particles only affects the inductance at the low frequency of operation since they are transparent at the high frequency, and therefore the effective lower frequency in the absence of beads can be reconstructed from the higher frequency. The difference of the actual and reconstructed lower frequencies cancels the system drift and corresponds to shift only due to the magnetic content. In addition, this approach obviates the need of a replica reference, since the sensor acts as its own self-reference, halving the required chip area and power consumption per sensing unit. No external magnets or moving parts are needed. We implement a prototype 2×2 array of the transformer-based drift-cancelling magnetic sensor in a standard CMOS 65nm process. The sensor operates at 1.44GHz and 3.65GHz and uses a 1:1 transformer with k of 0.73 and 4.2nH inductance per coil. Each sensor runs off a 1V supply and its bias current can be adjusted from 3 to 30mA, enabling each cell to consume as little as 3mW of power. On-chip digital dividers divide the oscillation frequency by 32, allowing for basic frequency counting circuitry to perform sensor readout. Both sides of the transformer are interleaved and laid out as common-centroid to maximize matching between inductance, capacitance, and active devices. The phase-noise was measured to be -130dBc/Hz at a 1MHz offset for the 1.44GHz frequency. Figure 10.7.2 shows a block diagram of the sensor array design.

We alternate switching the sensor between low and high frequencies, counting each for one second at a time, over an 11hr time period to test the frequency tracking and reconstruction capabilities of the system. Figure 10.7.3 shows the low frequency reconstructed from the high frequency data overlaid on top of the measured low frequency, demonstrating the excellent tracking ability of the sensor. Figure 10.7.4 shows time-domain waveforms of the measured low, reconstructed low, and difference frequencies with magnetic beads over the sensor and after they are removed. As can be seen, the reconstructed signal captures the drift content and noise of the lower frequency. Note that the high frequency shifts slightly upwards when beads are introduced. This is due to the fact that the frequency is not high enough for the beads used to be completely transparent, and they instead operate in the regime where the effective inductance is decreased [4]. This leads to an improvement in the effective SNR, since the two frequencies shift in opposing directions due to magnetic content, but in the same manner in response to sensor noise. The frequency noise-floor of the drift-compensated signal was measured to be 500Hz, corresponding to a 0.35ppm detection capability. We measure differing amounts of 4.5μm Dynabeads to characterize sensor response, linearity, and dynamic range, also shown in Fig. 10.7.4. A single bead can be easily resolved by the sensor owing to the drift-cancellation, and excellent linearity is achieved with a dynamic range of at least 62dB, limited only by the maximum number of beads that we measured.

Each sensing site is 250×250μm^2, offering adequate area for DNA, protein, and cell experiments. We perform a DNA detection assay to demonstrate the viability of our sensor to be used in in-vitro experiments: a capture DNA strand is attached to the sensing surface and the presence of a complementary target DNA strand binds the capture strand to a probe strand labeled with a 1μm magnetic marker. The magnetic markers are thus anchored to the sensing surface by the target strand. Figure 10.7.5 shows a diagram of the experiment, a photo of the sensor surface with bound beads, and the measured sensor response indicating that the sensor was able to successfully detect and measure the presence of the target DNA.

Acknowledgments:
The authors thank K. Mauser and N. Scianmarello for help with sample preparation.

References:
[1] G. Li, et al., "Detection of Single Micron-Sized Magnetic Bead and Magnetic Nanoparticles Using Spin Valve Sensors for Biological Applications," *Journal of Appl. Phys.,* vol. 93, no. 10, pp. 7557-7559, 2003.
[2] H. Wang, et al., "A Frequency-Shift CMOS Magnetic Biosensor Array with Single-Bead Sensitivity and No External Magnet," *ISSCC Dig. Tech. Papers,* pp. 438-439, 2009.
[3] J.-C. Chien, and A.M. Niknejad, "Oscillator-Based Reactance Sensors with Injection Locking for High-Throughput Flow Cytometry Using Microwave Dielectric Spectroscopy," *IEEE JSSC*, vol. 51, no. 2, pp. 457-472, 2016.
[4] C. Sideris and A. Hajimiri, "An Integrated Magnetic Spectrometer for Multiplexed Biosensing," *ISSCC Dig. Tech. Papers,* pp. 300-301, 2013.
[5] T. Mitsunaka, et al., "CMOS Biosensor IC Focusing on Dielectric Relaxations of Biological Water With 120 and 60 GHz Oscillator Arrays," *IEEE JSSC*, vol. 51, no. 11, pp. 2534-2544, 2016.
[6] K.-H. Lee, et al., "CMOS Capacitive Biosensor with Enhanced Sensitivity for Label-Free DNA Detection," *ISSCC Dig. Tech. Papers,* pp. 120-121, 2012.

 978-1-5090-4940-0/18/$31.00

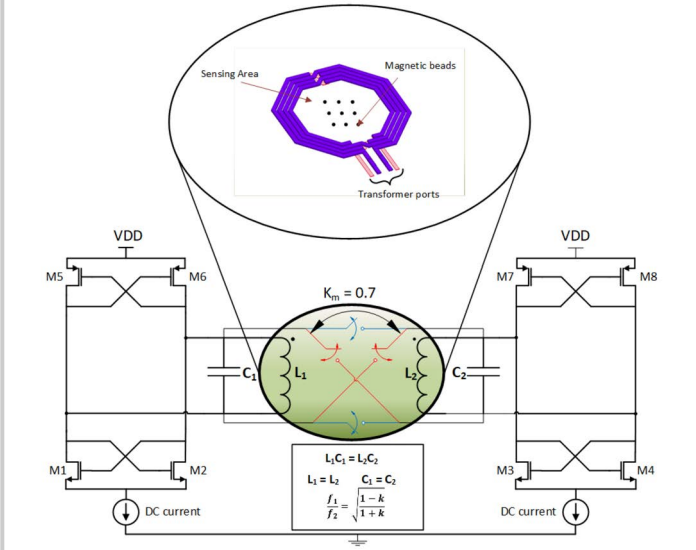

Figure 10.7.1: Dual-resonance transformer-based magnetic sensor schematic.

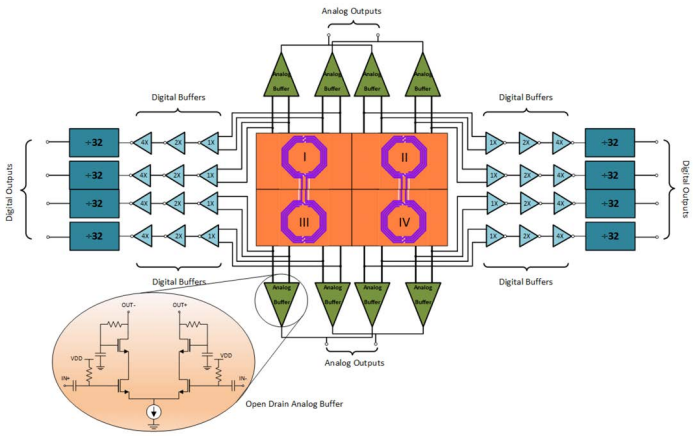

Figure 10.7.2: 2×2 magnetic sensor array system block diagram.

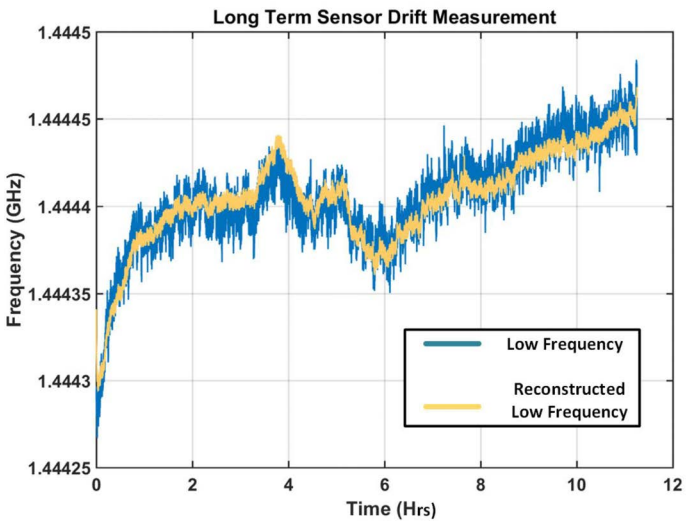

Figure 10.7.3: Demonstration of long-term drift cancellation over 11-hour measurement period.

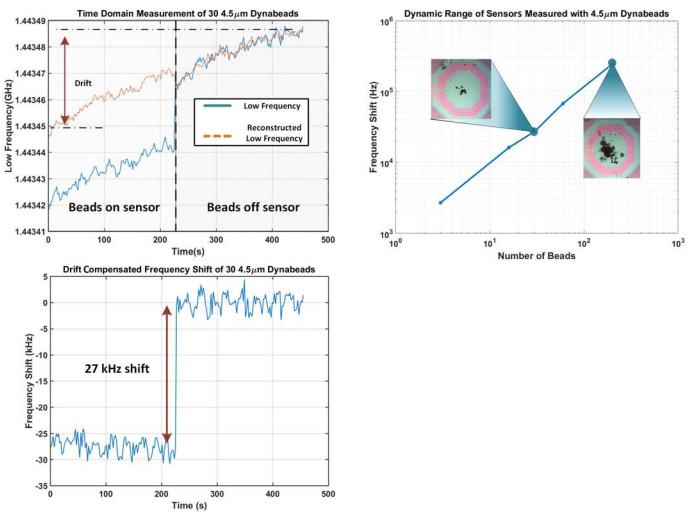

Figure 10.7.4: Time-domain sensor response to magnetic bead and sensor dynamic range characterization.

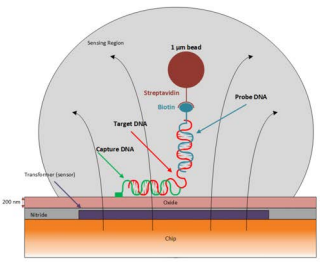

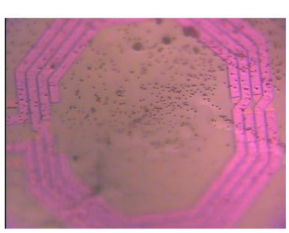

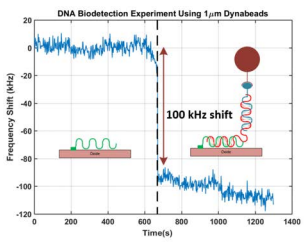

Sequences Used in Experiment:

Capture DNA: GTTGTTGGGGCTGCTGTTGTCTGGCTGGCTGTGGTGGTGGCT

Probe DNA: GCTGCTTCGTGGGTGGTCGGTGTGGATTGCGTGGTCGTCTTG

Target DNA: CAAGACGACCACGCA ATCCACACCGACCACCCACGAAGCAGC CAGCACAGCCACCACCACAGCCAGCCAGACAACAGCAGCCCC AACAAC

Figure 10.7.5: In-vitro DNA detection experiment and sensor response.

	[2]	[3]	[5]	[6]	This work
Sensor Type	LC (Inductive)	LC (Injection Locked)	LC (Inductive)	Capacitive	**LC (Transformer)**
Technology	0.13 μm	65 nm	65 nm	0.35 μm	**65 nm**
Power	165 mW	65 mW	12.2 mW (@60 GHz)	2.34 mW	**5 mW**
Sensitivity (ppm)	0.23 ppm	1.25 ppm	2.67 ppm	N/A	**0.3 ppm**
Reference Required	Yes	Yes	N/A	Yes	**No**
Sensor Active Area*	0.6 mm^2	0.212 mm^2	0.014 mm^2	0.99 mm^2	**0.17mm^2**
Frequency	1.01 GHz	6.5/11/17/30 GHz	60GHz and 120GHz	N/A	**1.4/3.6 GHz**
Temperature Control Required	Yes	Yes	Yes	N/A	**No**
Dynamic range	N/A	52 dB	N/A	N/A	**>62 dB**

** Sensor and reference cell area*

Figure 10.7.6: Performance comparison summary.

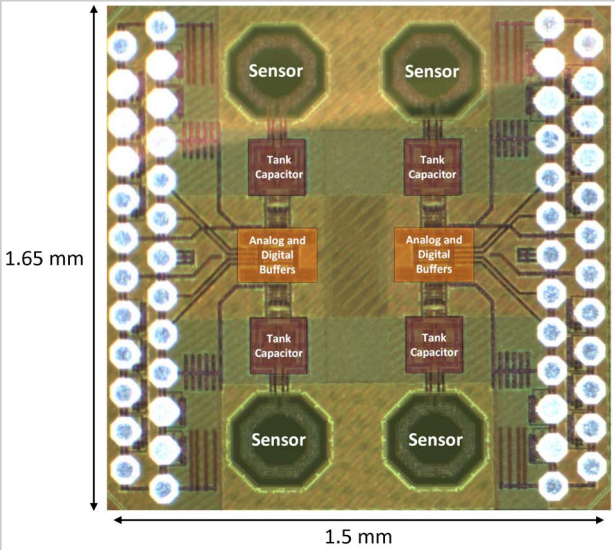

Figure 10.7.7: 2×2 chip sensor array die photo.

978-1-5090-4940-0/18/$31.00